Supplementary Information

Modulation Doping via a 2D Atomic Crystalline Acceptor

Yiping Wang,[1†] Jesse Balgley,[2†] Eli Gerber,[3] Mason Gray,[1] Narendra Kumar,[1] Xiaobo Lu,[2] Jia-Qiang Yan,[4,12] Arash Fereidouni,[5] Rabindra Basnet,[5] Seok Joon Yun,[6] Dhavala Suri,[7] Hikari Kitadai,[8] Takashi Taniguchi,[9] Kenji Watanabe,[9] Xi Ling,[8] Jagadeesh Moodera,[7] Young Hee Lee,[6] Hugh O. H. Churchill,[5] Jin Hu,[5] Li Yang,[2,10] Eun-Ah Kim,[11] David G. Mandrus,[4,12] Erik A. Henriksen,[2,10*] Kenneth S. Burch[1**]

E-mail: ks.burch@bc.edu,henriksen@wustl.edu

Contents

1 Raman scattering and photoluminescence

A WITec system inside Ar environment glovebox[1] has automatic mapping with a 532 nm laser, 1 μm spot size and 1800 g/mm grating is used in this experiment. The laser power is 300 μW, the integration time is 25 s and the step size is 0.3 μm for all Raman maps. Due to additional disorder, the CVD graphene signal was weaker and thus we employ 300s integration time. The EuS and EuS/$RuCl_3$ measurement are performed with 100μW with 300s integration time.

2 Device fabrication and transport

Devices were fabricated using a dry van der Waals stacking technique[2] to sequentially pick up and stack layers of graphene, hexagonal boron nitride, α-$RuCl_3$, and $CrCl_3$, using either poly(bisphenol a) carbonate (PC) or polypropylene carbonate (PPC) films as the adhesive layer. $CrCl_3$ flakes were only exposed to a N_2 atmosphere,[3] with the rest assembled in air. Cr/Au top gate and edge contacts were patterned by standard e-beam lithography.[2] Transport measurements were carried out in a Quantum Design Physical Properties Measurement System (PPMS) at Washington University in St. Louis.

3 Material Growth

Single crystals of α-$RuCl_3$ were grown using a vapor transport technique from phase pure commercial α-$RuCl_3$ powder.[4] Single crystals of $CrCl_3$ are grown by recrystallizing $CrCl_3$ powder in an evacuated quartz tube with temperature gradient 650-550 °C for one week. EuS (10 nm) was deposited at room-temperature at 10^{-8} torr, on freshly cleaved $RuCl_3$ surface, using an e-beam evaporation technique. Monolayer CVD graphene was grown on a copper foil via low pressure CVD (details in SI).

4 Peak fitting

To accurately represent the phonon frequencies and amplitudes, we fit the Raman spectra with the Voigt function

$$I(\omega, \sigma, \Gamma, A) = \int_{-\infty}^{\infty} G(\omega', \sigma) L(\omega - \omega', \Gamma, A) d\omega'$$

which is a convolution of a Gaussian and a Lorentzian. Here the Lorentzian represents a phonon mode and we use a Gaussian to account for the instrumental resolution. The Gaussian width $\sigma = 1$ cm^{-1} is determined by the central Rayleigh peak. Γ is the phonon width and A is phonon amplitude.

For the mlg G peak spectra, we choose to fit in the range of 1550–1650 cm^{-1}, using a constant background and three-Voigt peaks to capture the a broad background that appears in this energy range from the α-$RuCl_3$ itself, as well as the presence of both shifted and unshifted G-peaks. For the mlg and blg 2D peak spectra, we fit from 2650–2750 cm^{-1}, with a constant background and two-Voigt peaks, for both the shifted and unshifted 2D peaks. For the blg 2D peak, we used four-Voigt peaks with a constant background to capture the four characteristic blg 2D peaks (1A, 1B, 2A, 2B). We plot Raman shift distributions against $2D_{1A}$ peak, and use this peak to calculate blg carrier density, as this peak follows the same trend as the mlg 2D peak.[5]

5 Determination of strain and doping from Raman

Raman phonon frequencies in graphene are sensitive to both doping and strain. However, these two effects can be separated via correlation decoupling analysis of the G and 2D frequencies.[5–7] In the main text Fig. 1c & Fig. 4a, we use this analysis to calculate the doping level in the mono and bilayer graphene of our heterostructures. We denote the G and 2D peak frequencies for free standing graphene as: $(\omega_G^0, \omega_{2D}^0) = (1581.6 \pm 0.2 \text{ cm}^{-1}, 2676.9 \pm 0.7 \text{ cm}^{-1})$

and the frequency shifts from these intrinisic values by $(\Delta\omega_G, \Delta\omega_{2D})$. It is well established that the degree of shift due to doping and strain is different for the graphene G and 2D peaks.[6,8] From electronic gating measurements and theoritical calculations,[5,6,9] the effect of hole doping on the graphene G and 2D peak frequency is quasi-linear with a relationship: $(\Delta\omega_G^{doping}/\Delta\omega_{2D}^{doping}) = tan(\theta_1)$=0.75 (The red arrow line in Fig. S1a and doping line in the main text Fig. Fig. 1c and Fig. Fig. 4a). Exfoliated graphene always shows uniaxial strain on the G and 2D frequencies, which follow $(\Delta\omega_G^{strain}/\Delta\omega_{2D}^{strain}) = tan(\theta_2) = 2.2$[6] (strain line in Fig. S1a, Fig. 1c and 4a). Next we use $(\omega_G^0, \omega_{2D}^0)$ to set the intercept of the strain and doping lines in the (ω_G, ω_{2D}) space. Thus the shifts in the G and 2D peaks are determined by (see Fig. S1):

$$l_D * sin(\theta 1) + l_S * sin(\theta 2) = \Delta\omega_{2D}$$
$$l_D * cos(\theta 1) + l_S * cos(\theta 2) = \Delta\omega_G$$

By inverting this equation, we can take the measure $(\Delta\omega_G, \omega_{2D})$ and determine the strain and Fermi level. A downward (upward) projected vector along the strain line Fig. S1a, Fig. 1c & 4a)+ corresponds to tensile (compressive) strain, while along the doping line the vector is always projected to the upward direction for both n and p type doping.

To determine the precise doping level, we employ the results of three independent measurements and a theory calculation shown in Fig. S1b. Specifically, the increase of $\Delta\omega_G$ is proportional to the shift of Fermi level in the high charge carrier limit ($E_F > 100$ meV). Using a linear fit to the ω_G Vs E_F, we can then extract the Fermi energy at each shifted G peak frequency(Fig. S1a).

$$E_F = \Delta\omega_G^{puredoping}/\alpha$$
$$= l_D * sin(\theta_1)/\alpha$$

Here, α is the linear fitting of $\Delta\omega_G$ and E_F for mlg. From the average of four electric gating

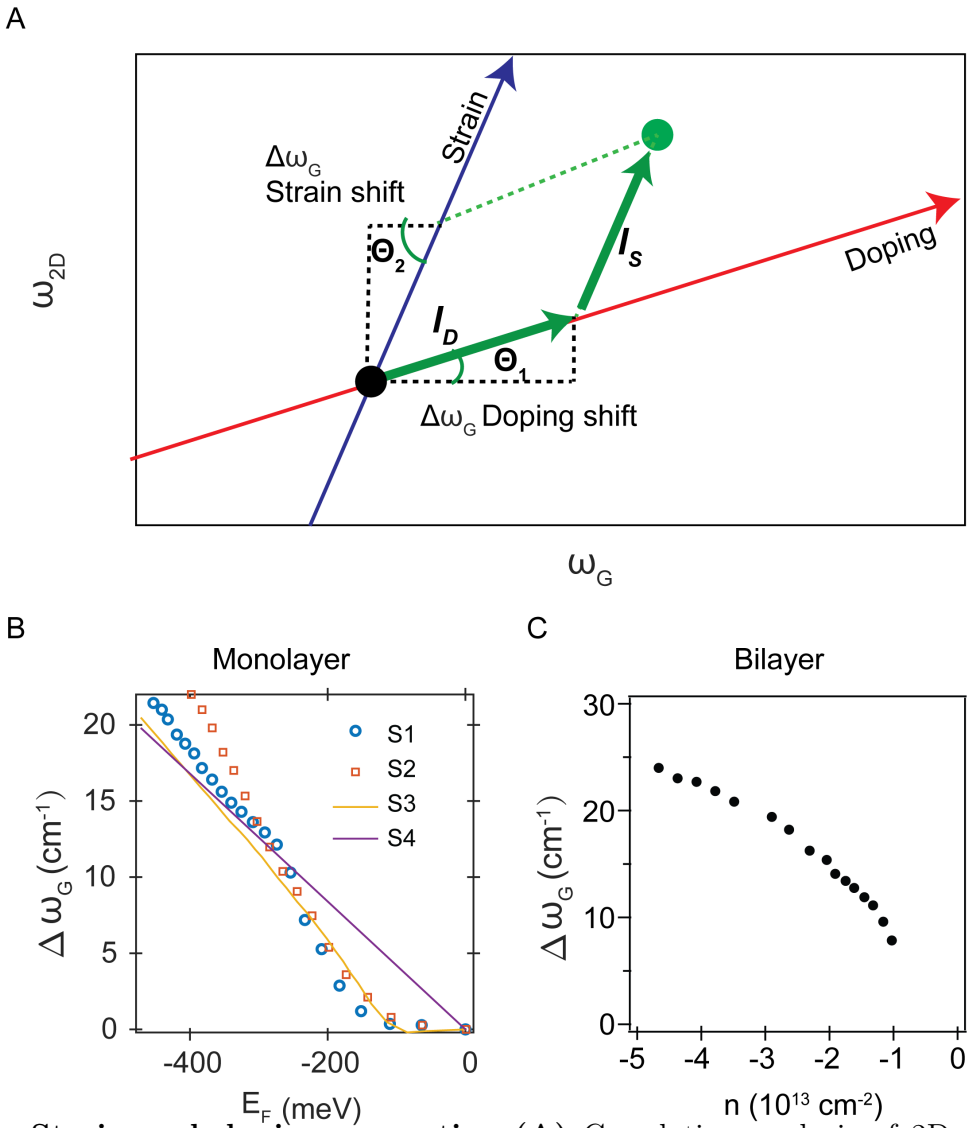

Figure S1: **Strain and doping separation (A)** Correlation analysis of 2D and G frequencies to separate the frequency shifts from strain and doping. Data adapted from Refs.[5,7,9,10] **(B)** and Ref.[11] **(C)** for converting Raman G and 2D peak shifts in monolayer and bilayer graphene, respectively, to Fermi energy shifts and doping level.

studies (ref.[5,7,9,10]), we set α = -45.7 eV/cm^{-1}. Therefore, after converting E_F to carrier density we can use the expression below to get the carrier densities of monolayer graphene. As for strain, it also linearly depends on the G peak frequency shift.

$$
\begin{aligned}
p &= \frac{1}{\pi}\frac{E_F}{\hbar * v_F}^2 \\
&= \frac{1}{\pi}(\frac{sin(\theta 1)}{\alpha * \hbar * v_F})^2 * l_D^2 \\
\epsilon &= \Delta\omega_G^{purestrain}/s \\
&= \frac{sin(\theta 2)}{s} * l_S
\end{aligned}
$$

Here, v_F is the Fermi velocity, s is the percent of strain. For uniaxial strain s is -23.5 $cm^{-1}/\%$ and for biaxial strain s is -69.1 $cm^{-1}/\%$.

In the bilayer graphene case, the carrier density to G peak shift relationship is slightly different from monolayer graphene. To convert Raman peak shifts in bilayer graphene to doping levels, we first followed Ref.[6] to project the peak shift values along the doping axis, as we did with monolayer graphene, then utilized the results from Ref.[11] Fig. S1c, to convert the G peak shift to hole doping level.

6 Theory: DFT

The DFT calculations are performed within the generalized gradient approximation (GGA) using Perdew-Burke-Ernzerhof (PBE) functional implemented in Vienna Ab initio Simulation Package (VASP).[12] A plane-wave basis set with a kinetic energy cutoff of 450 eV, and a $4 \times 3 \times 1$ k-point sampling grid is adopted to a heterostructure supercell with cell constant of 12.03 Å. The geometric structure of heterostructures are relaxed by fixing hBN and graphene layers to the α-$RuCl_3$ lattice constant (6.02 Å) with fully relaxed force of α-$RuCl_3$. This relaxation scheme better mimics the band alignment and charge transfer since the work

function of graphene is not sensitive to strain and the strain effect on the wide gap of hBN is small. The proper super cell of α-$RuCl_3$ ($2 \times 2 \times 1$) and for hBN ($5 \times 4 \times 1$) and graphene ($5 \times 4 \times 1$) are used to reduce the stress induced by the lattice mismatch between materials while balancing the computational burden.[13] The vacuum distance is set to be around 18 Å along the z-direction to avoid spurious interactions. The vdW interaction is included by the DFT-D2 method[14] and spin orbit coupling (SOC) is always considered. The choice of Hubbard $U = 2.4$ eV and Hund $J = 0.4$ V for Ru^{3+} ions is based on previous studies.[15,16]

7 Theory: MINT

The *ab initio* MINT calculations were carried out within the total-energy plane wave density-functional pseudopotential approach, using Perdew-Burke-Ernzerhof generalized gradient approximation functionals[17] and optimized norm-conserving Vanderbilt pseudopotentials in the SG15 family.[18] Plane wave basis sets with energy cutoffs of 30 Hartree were used to expand the electronic wave functions. We used fully periodic boundary conditions and a single unit cell of α-$RuCl_3$ with a $6 \times 4 \times 1$ k-point mesh to sample the Brillouin zone. Electronic minimizations were carried out using the analytically continued functional approach starting with an LCAO initial guess within the DFT++ formalism,[19] as implemented in the open-source code JDFTx[20] using direct minimization via the conjugate gradients algorithm.[21] All unit cells were constructed to be inversion symmetric about $z = 0$ with a distance of ≈ 60 Bohr between periodic images of the α-$RuCl_3$ surface, using Coulomb truncation to prevent image interaction.

8 Evidence for charge transfer in MBE grown EuS

EuS is a magnetic semiconductor with a low work function (3.3 eV) than is routinely used in various spintronic and proximity heterostructures. It has a ferromagnet transition temperuture of 13K.[22] We began with a 10nm EuS film grown atop of bulk α-$RuCl_3$ and ensured

both components were intact by SQUID measurements. As shown in Fig. S2a,b we observe the ferromagnetic transition for the heterostructure at the T_c of EuS (13 K). Furthermore the bulk antiferromagnetic transition of α-$RuCl_3$ is also seen at 8K . The hysteresis loop at 2K in Fig. S2c further confirms the quality of EuS/$RuCl_3$ heterostructure. To determine if charge transfer occurred we again turn to Raman spectrocopy to ensure no effects of fabrication. Indeed, bare EuS has easily measurable room temperature Raman response at 30.4 meV and the second and third harmonic peaks at 60.8 and 91.2 meV.[23] However, this response becomes suppressed when EuS is significantly doped by charge transfer that removes the real optical transition by Pauli blocking.[24]

Consistent with α-$RuCl_3$ significantly doping EuS, the Raman results in (Fig. S2d) show only the EuS phonons at 30.4 meV and 60.8 meV when grown on sapphire, whereas the EuS/$RuCl_3$ heterostructure only shows the α-$RuCl_3$ phonons. This provides the evidence that EuS is doped by α-$RuCl_3$ and shifts the Fermi level down to where the laser cannot excite electrons to the conduction band (greater than 2.33 eV). We further confirmed this by attaching leads via Ag epoxy and found the room temperature resistivity of EuS/$RuCl_3$ heterostructure is $\rho = 4.5 \times 10^{-6}$ Ω cm, which is four orders of magnitude smaller than bulk EuS resistance $\rho = 1.9 \times 10^{-2}$ Ω cm.[25] We note that bulk α-$RuCl_3$ of similar thickness revealed a resistance three orderds of magnitude larger then the heterostructure. This evidence for large charge transfer is consistent with our *ab initio* ''mismatched interface theory'' (MINT)[26] calculations that predict an induced hole density of 6.5×10^{13} cm^{-2} in EuS.

9 Evidence for charge transfer into CVD grown WSe_2

Monolayer WSe_2 has a direct band gap and strong exciton binding energy. As the relatively sharp photoluminescence (PL) emission can be sensitive to the chemical potential. In particular for neutral WSe_2 the exciton is observed, whereas when doped it forms trions.[27] Thus the exciton emission can be used to detect the carrier type (doping level) and density in

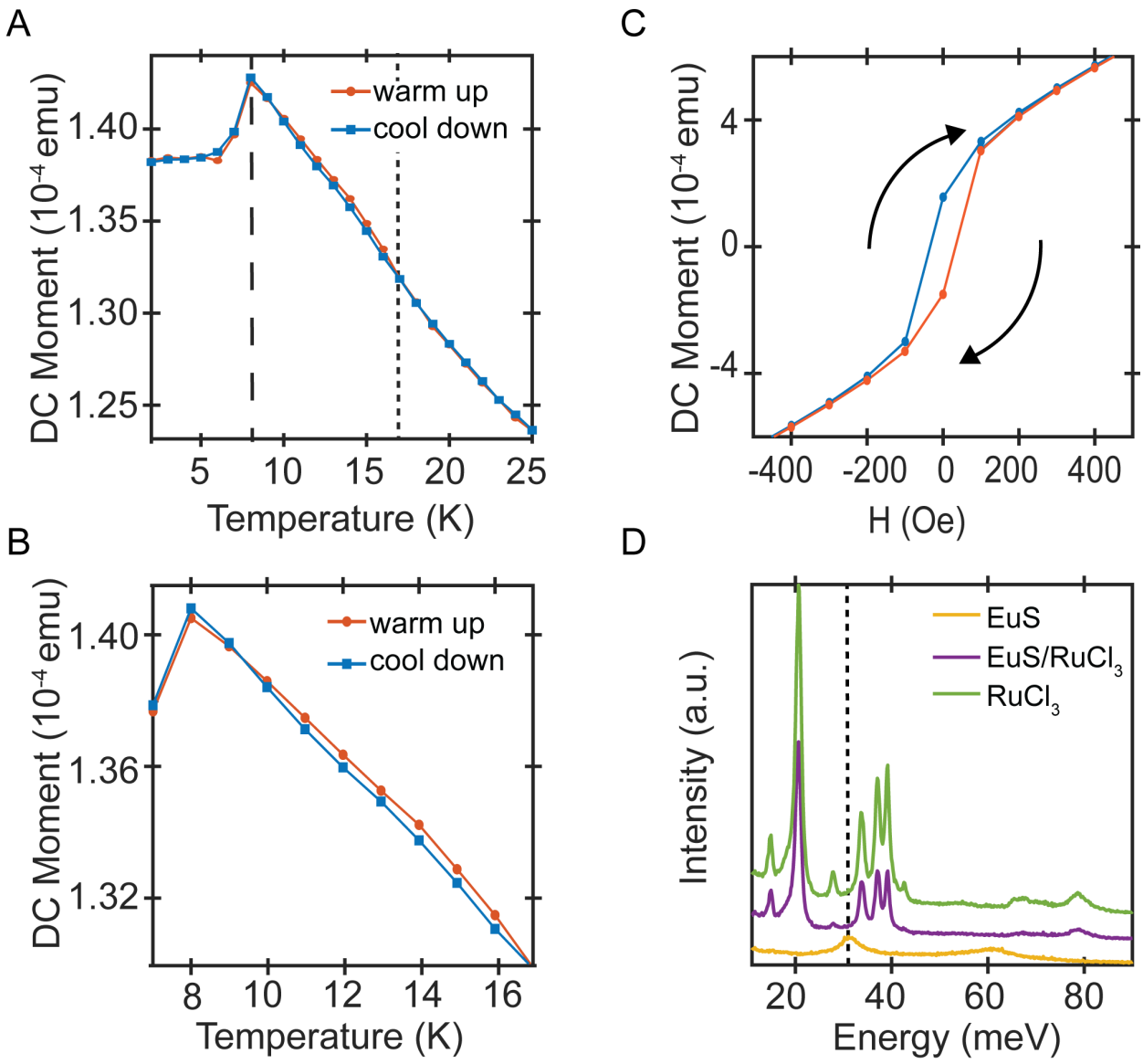

Figure S2: $EuS/RuCl_3$ heterostructure **(A)** Temperature dependent DC moment of $EuS/RuCl_3$ heterostructure. The dash line is the Neel temperature of α-$RuCl_3$, the dot line is the Tc of EuS. **(B)** Zoom in of **(A)**. **(C)** Field dependent DC moment at 2K of $EuS/RuCl_3$ heterostructures. **(D)** Raman spectra of EuS,α-$RuCl_3$ and $EuS/RuCl_3$ heterostructures.

monolayer WSe_2.[28] To investigate this possibility, we employed CVD grown and transferred a α-$RuCl_3$ flake on top. The PL from the bare WSe_2 peaks at 1.65 ev, where the region covered by α-$RuCl_3$ has significantly narrowed and shifts to 1.665 eV (Fig. S3a). This is consistent with previous reports where n-type or intrinsic WSe_2 has a weaker and lower energy PL emission, while hole-bound trions in p-type WSe_2 have stronger and blue-shifted emission lines. To exclude the possibility of that the redshift results from strain, we use Raman spectra to check the phonons in the $WSe_2/RuCl_3$ heterostructure. As shown in (Fig. S3b), the phonon frequencies of $WSe_2/RuCl_3$ heterostructure can overlap with either α-$RuCl_3$ or WSe_2. This indicates that the strain can be negligible and cannot result in the PL shift. All of the above points to α-$RuCl_3$ accepting electrons from the WSe_2.

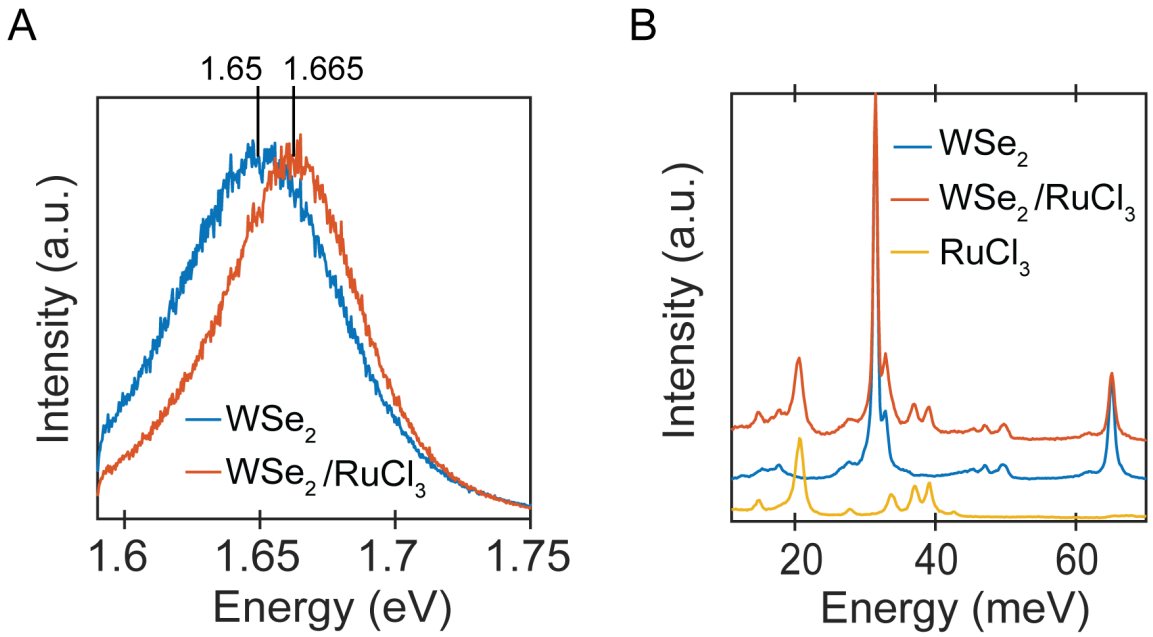

Figure S3: $WSe_2/RuCl_3$ heterostructure **(A)** Room temperature PL of pure WSe_2 and $WSe_2/RuCl_3$. **(B)** Room temperature Raman spectra of WSe_2, α-$RuCl_3$ and $WSe_2/RuCl_3$.

10 Charge transfer into CVD graphene

The charge transfer between α-$RuCl_3$ and graphene also can be realized in CVD graphene/$RuCl_3$ heterostructures, crucial for eventual scale-up. To demonstrate this we gently exfoliate thin

α-$RuCl_3$ flakes on top of a CVD graphene film on SiO_2/Si substrate(see method). As shown in Fig. S4, the Raman from the CVD graphene revealed a G peak frequency lower than 1590 cm^{-1}, but when moving the laser to the region with the CVD graphene/$RuCl_3$ heterostructure the peak shifts to 1617 cm^{-1}. Thus it is clear that similar doping levels can be achieved in CVD graphene films. However due to the transfer process this CD graphene was more disordered, resulting in lower overall Raman signals.

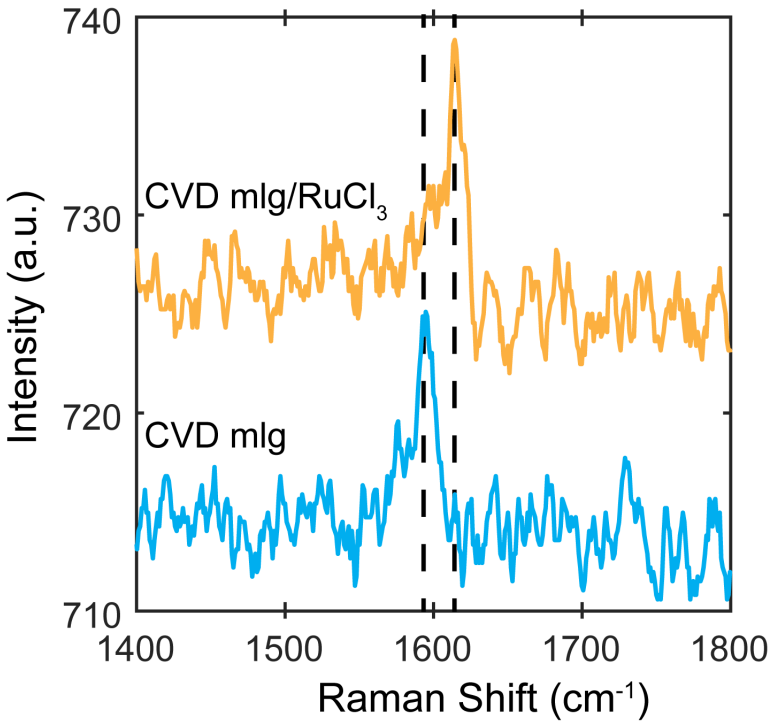

Figure S4: Raman spectra comparison of CVD graphene (Blue line) and CVD graphene/$RuCl_3$ heterostructure(Yellow line). A shift of the G peak consistent with entirely exfoliated structures indicates CVD graphene can be equally well charged by α-$RuCl_3$.

11 Optoelectronic response of graphene/α-$RuCl_3$heterostructures

Graphene can exhibit both photothermal and photovoltaic responses. The former is driven by electron temperature gradient and the later is generated by built-in electric fields. Both can be enhanced at high carrier densities but suppressed at the charge neutral point.[29] As such the photovoltage can be useful in detecting charge in homogeniety and the presence of

homojunctions in graphene. As shown in the main text (Fig. 2f) bottom, the region of the device under the α-$RuCl_3$ reveals a strong photovoltage at the interface which is insensitive to gate voltage. This is consistent with a photovoltaic effect resulting from the strong p-p' junction. Whereas the bare graphene reveals some signal due to inhomogenous doping, which can be nuetralized by the gate. Further confirmation that the signal from the edge of the α-$RuCl_3$ region is due to the photovoltaig effect is the power dependence. Namely as shown in (Fig. S55a), the response to power is strictly linear. In addition, the fact that this results from a built-in field is further supported by the polarization dependence seen in (Fig. S5b). Specifically the response is maximized for light polarized along the direction normal the to edge of the α-$RuCl_3$ which is parallel to the built-in field from the charge inhomogeniety in the graphene.

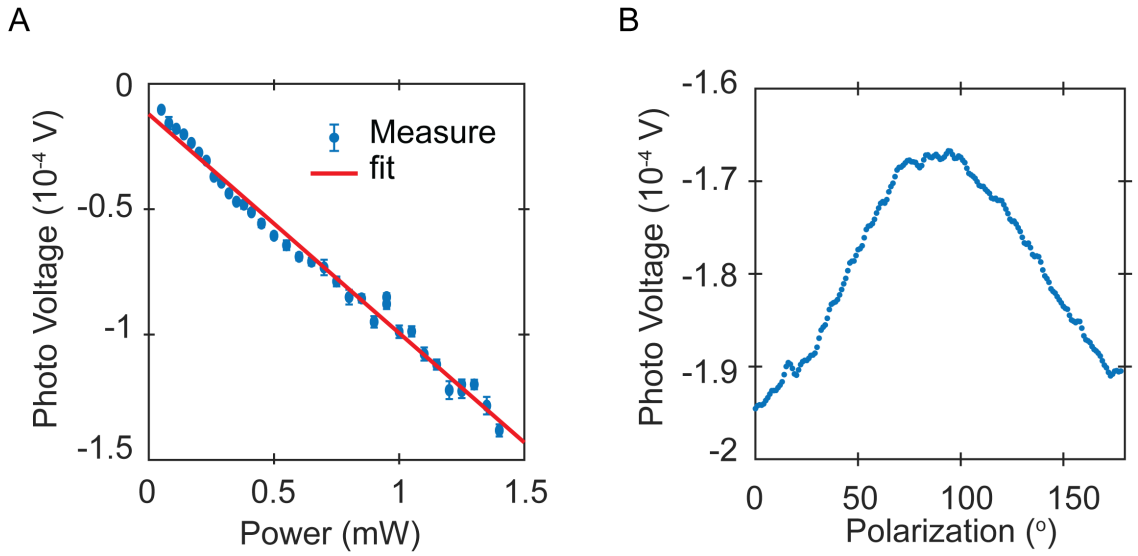

Figure S5: **(A)** power dependent photovoltage measurement of mlg/$RuCl_3$. **(B)** polarization dependent photovoltage measurement of mlg/$RuCl_3$

Electronic transport

(Fig. S6a) shows an optical micrograph of device D5, whose conductivity at $T = 10$ K is shown in the main text. This device features four interior contacts used to extract the zero-field resistivity, which is shown in (Fig. S6b) as a function of temperature and displacement field D. As in the conductivity linecut from Fig. 3E in the main text, the resistivity shows no sign of a Dirac peak, and increases monotonically with D indicating the graphene is highly hole doped by the adjacent α-$RuCl_3$.

Magnetoresistance measurements reveal high frequency Shubnikov-de Haas oscillations (SdH) from a large population of holes (Fig. S6c). Beating is observed in the SdH traces, from which we extract two frequencies, B_F, via a Fourier transform (Fig. S6d). Each frequency corresponds to a carrier density $p = gB_F/\phi_0$ where $g = 4$ counts the spin and valley degeneracies in graphene and ϕ_0 is the magnetic flux quantum. The resulting densities are plotted vs the applied gate voltage, and reveal one population of holes that disperses with D (black circles) and a second that is independent of V_g (blue circles). The two densities are equal at $D = 0$. We attribute the non-dispersing contribution to ungated regions of the graphene that exist around the electrical contacts, which still contribute to the magnetoresistance but where the Fermi energy does not change with D. This leaves a single population of holes that respond to the gate voltage, indicating that in a clean sample, the α-$RuCl_3$ strongly and uniformly hole dopes the graphene.

12 Interference correction

Raman scattering can be enhanced or suppressed by the interference from thin layers in the heterostructure. The change in the Raman response from intereference can be calculated by applying Fresnel's Law to the thin films and summing up the contribution of different layers.[30] In the main text, we show hole doping in graphene are detected via graphene G peak shift. Thus, the wavenumber dependent enhancement contribution from α-$RuCl_3$ to

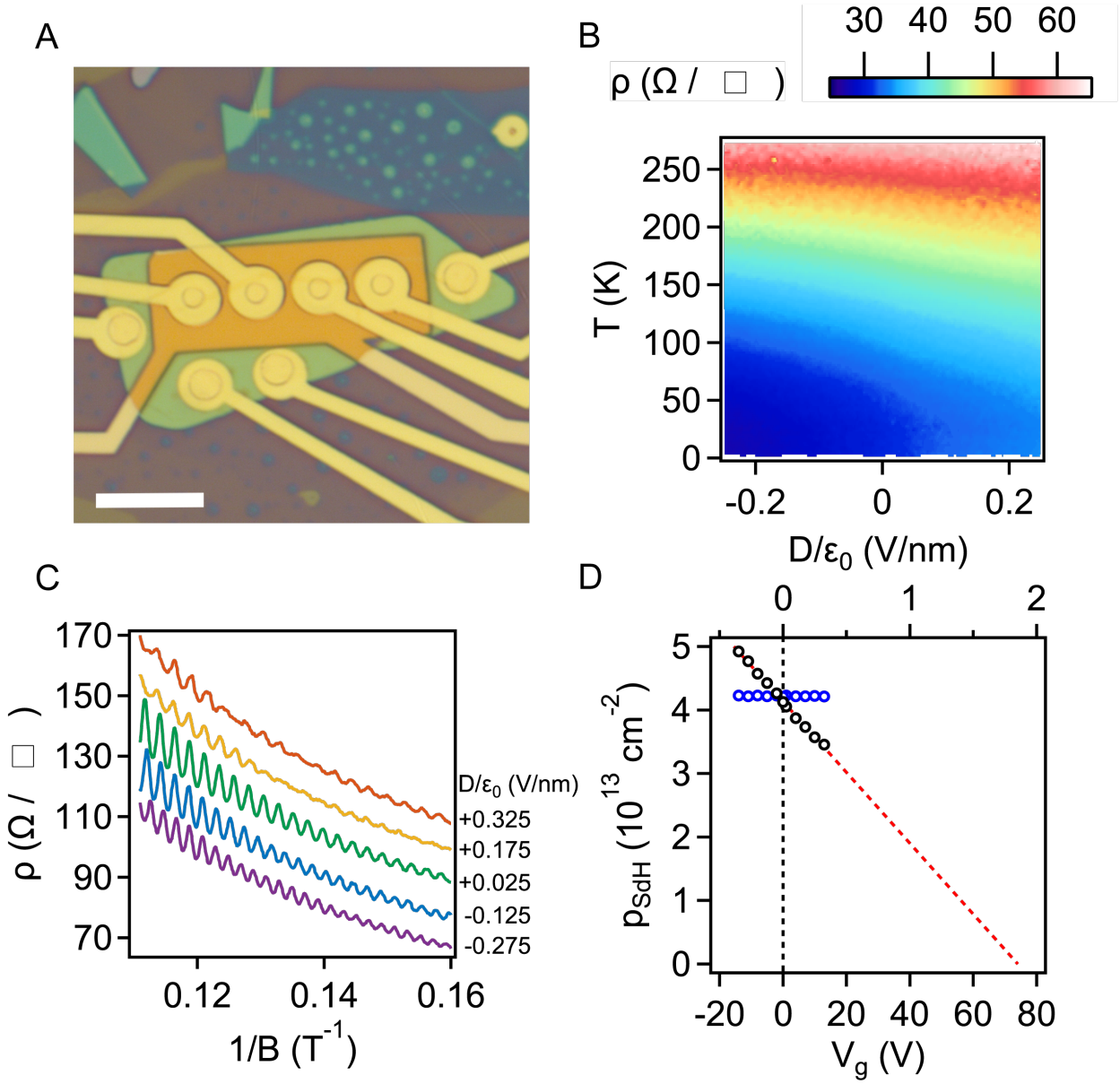

Figure S6: **Electronic transport (A)** Optical micrograph of device D5. **(B)** Map of gate voltage and temperature dependence of the resistivity of D5. **(C)** SdH oscillations at various displacement fields. **(D)** Carrier densities extracted from SdH oscillations. The two unique frequencies found in each SdH trace reveal two populations of holes (black & blue circles) from gated and ungated regions in device, respectively, but both reveal that the graphene is highly doped by the α-$RuCl_3$.

graphene layer becomes important. Here, via dividing the mlg/$RuCl_3$ response with the enhancement factor from α-$RuCl_3$, one can get the not-enhanced spectrum (Fig. S7). It is very different to the G peak response of pure mlg on SiO_2/Si substrate. This indicates that

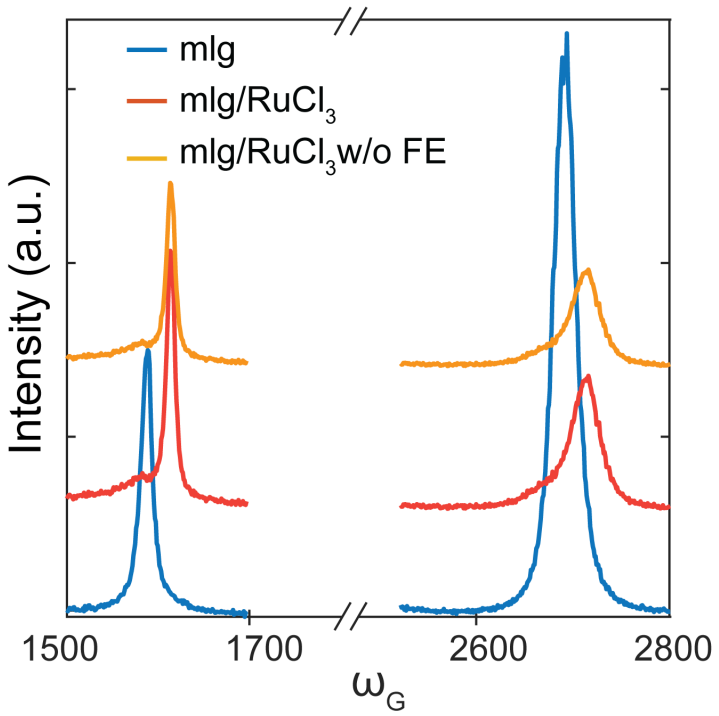

Figure S7: **Optical correction** A comparison of the measured Raman from mlg on SiO_2 (blue) with graphene on thin α-$RuCl_3$. After dividing by the intereference factor of enhancement(FE) due to the presence of α-$RuCl_3$ (yellow) we find the G and 2D peaks do not shift their positions.

the G and 2D peak shifts in the heterostructure region is not caused by the stacking layers enhancement. Furthermore we find that the peak positions of the G and 2D peaks is not influenced by the itnereference.

13 Range of doping in graphene/α-$RuCl_3$heterostructures

A crucial aspect of the the heterostructures presented is the overall uniformity. One measure presented in the main text is the presence of neutral puddles inside doped regions. A second is the range of resulting doped values. To access the range of induced dopings, for each device we made a histogram of the local doping level at each point in our Raman maps. These are shown in (Fig. S8) for all the devices presented in the main text. In general we find the distribution of induced carrier densities to be well described by lorentzians whose half width at half maximum varies by $\delta p \approx 1$–5×10^{12} cm^{-2}. Perhaps not surprisingly, we

find the width for the hBN spaced region to be substantially smaller (i.e. more homogenous).

14 Doping spatial resolution

In the homogeneity map (Fig 3C), we mapped out the hereostructure region and find 95% homogeneity. Our step size is d = 300nm, the step radius is r = 150nm. Therefore, each step covers region $A = \pi * r^2 = 70685.8\, nm^2$. *In each step, 5% area is inhomogeneous, which means the inhomogeneity region is* $A_0 = 5\%*A$. *The inhomogeneous region results from the charge transfer spatial range. We then calculate the short range charge transfer resolution* d_0 *from* A_0, *where* $d_0 = 2 * \sqrt{A_0/\pi} = 67nm$.

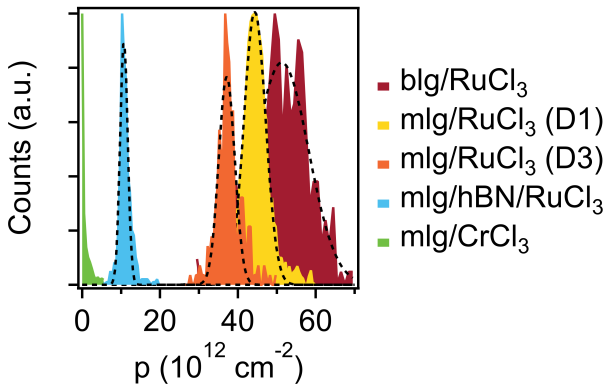

Figure S8: **Doping distributions** Histogram of doping distributions from scanning Raman maps. Black dashed lines represent Gaussian fits.

15 CVD Growth and Fabrication

The copper foil (Alfa Aesar) was pre-treated in Ni etchant (Transene) to remove any coatings or oxide layers from its surface. The tube furnace was evacuated to a read pressure of 200 mTorr with a constant flow of H_2 (10 sccm). Prior to growth, the foil was annealed at 1010 °C (ramp rate 25 °C/min) for 35 min. Growth was done at 1010 °C with 68 sccm of H2 and 3.5 sccm of CH_4 for 15 min.

Table S1: Maximum achieved graphene charge densities $n_{\max}$ reported for different doping mechanisms, including α-$RuCl_3$ heterostructures, solid polymer electrolyte gating, ionic liquid gating, gating through an $SrTiO_3$ (STO) dielectric, and various atomic or molecular intercalation, adsorption, and functionalization methods. Values of the mobility μ at $n^* = 30 \pm 5 \times 10^{12}$ cm^{-1} are also listed where available.

Doping mechanism	$n_{\max}$ (10^{12} cm^{-2})	$\mu(\sim n^*)$ (cm^2 V^{-1} s^{-1})	Ref.
$RuCl_3$	-50	4900	Present work
	-38	1015	[31]
	-36	1900–6000	[32]
Solid polymer electrolyte gating	-400	2000	[33]
	±25	1500	[34]
	+60	N/A	[35]
	-30; +40	N/A	[7]
	±25	N/A	[36]
Ionic liquid gating	±50	30	[37]
	-4; +7	N/A	[38]
	-60	N/A	[10]
STO gating	-7; +11	N/A	[39]
$FeCl_3$ interc.	-580	N/A	[40]
KC_8 interc.	+134	N/A	[41]
Osmium adsorp.	-16	N/A	[42]
Tungsten adsorp.	+6	N/A	[43]
Indium adsorp.	+4.5	N/A	[44]
Ca + K adsorp.	+165	N/A	[45]
Chlorine func.	+15	N/A	[46]

Table S2: Summary of experimentally measured and theoretically calculated densities for different graphene/$RuCl_3$ heterostructures.

Sample	p (10^{12} cm^{-2})	Method
mlg/$RuCl_3$ (D1)	29.23	Raman
mlg/$RuCl_3$ (D2)	31.37	Raman
mlg/$RuCl_3$ (D3)	22.21	Raman
mlg/$RuCl_3$ (D5)	41.60	Transport
mlg/$RuCl_3$	39.29	DFT
mlg/$RuCl_3$ (0°)	30.20	MINT
mlg/$RuCl_3$ (30°)	24.47	MINT
mlg/hBN/$RuCl_3$ (∼5L hBN) (D3)	6.02	Raman
mlg/hBN/$RuCl_3$ (1L hBN)	23.75	DFT
mlg/hBN/$RuCl_3$ (2L hBN AA)	18.15	DFT
mlg/hBN/$RuCl_3$ (2L hBN AB)	16.15	DFT
blg/$RuCl_3$ (D2)	59.17	Raman
blg/$RuCl_3$ (AA)	44.185	DFT
blg/$RuCl_3$ (AB)	40.492	DFT

CVD graphene was removed from its copper film by applying a polymethyl methacrylate (PMMA) adhesion layer, followed by removal of the copper with Ni etchant for 2 h at 60 °C. The remaining PMMA/graphene structure was washed in water twice for 60 s, and after transfer to Si/SiO_2 the PMMA was dissolved in acetone vapors followed by isopropanol alcohol (IPA) and baked at 300 °C for 8 h in vacuum prior to stacking α-$RuCl_3$ on top.

16 References

References

(1) Gray, M. J. et al. A cleanroom in a glovebox. *Review of Scientific Instruments* **2020**, *91*, 073909.

(2) Wang, L.; Meric, I.; Huang, P. Y.; Gao, Q.; Gao, Y.; Tran, H.; Taniguchi, T.; Watanabe, K.; Campos, L. M.; Muller, D. A.; Guo, J.; Kim, P.; Hone, J.; Shepard, K. L.;

Dean, C. R. One-Dimensional Electrical Contact to a Two-Dimensional Material. *Science* **2013**, *342*, 614–617.

(3) Thompson, J. P.; Doha, M. H.; Murphy, P.; Hu, J.; Churchill, H. O. Exfoliation and Analysis of Large-area, Air-Sensitive Two-Dimensional Materials. *JoVE (Journal of Visualized Experiments)* **2019**, e58693.

(4) Banerjee, A.; Yan, J.; Knolle, J.; Bridges, C. A.; Stone, M. B.; Lumsden, M. D.; Mandrus, D. G.; Tennant, D. A.; Moessner, R.; Nagler, S. E. Neutron scattering in the proximate quantum spin liquid $\alpha-RuCl_3$. *Science* **2017**, *356*, 1055–1059.

(5) Das, A.; Chakraborty, B.; Piscanec, S.; Pisana, S.; Sood, A. K.; Ferrari, A. C. Phonon renormalization in doped bilayer graphene. *Phys. Rev. B* **2009**, *79*, 155417.

(6) Lee, J. E.; Ahn, G.; Shim, J.; Lee, Y. S.; Ryu, S. Optical separation of mechanical strain from charge doping in graphene. *Nature Communications* **2012**, *3*, 1024.

(7) Das, A.; Pisana, S.; Chakraborty, B.; Piscanec, S.; Saha, S. K.; Waghmare, U. V.; Novoselov, K. S.; Krishnamurthy, H. R.; Geim, A. K.; Ferrari, A. C.; Sood, A. K. Monitoring dopants by Raman scattering in an electrochemically top-gated graphene transistor. *Nature Nanotechnology* **2008**, *3*, 210–215.

(8) Gill, S. T.; Hinnefeld, J. H.; Zhu, S.; Swanson, W. J.; Li, T.; Mason, N. Mechanical Control of Graphene on Engineered Pyramidal Strain Arrays. *ACS Nano* **2015**, *9*, 5799–5806.

(9) Lazzeri, M.; Mauri, F. Nonadiabatic Kohn Anomaly in a Doped Graphene Monolayer. *Phys. Rev. Lett.* **2006**, *97*, 266407.

(10) Chen, C.-F.; Park, C.-H.; Boudouris, B. W.; Horng, J.; Geng, B.; Girit, C.; Zettl, A.; Crommie, M. F.; Segalman, R. A.; Louie, S. G.; Wang, F. Controlling inelastic light scattering quantum pathways in graphene. *Nature* **2011**, *471*, 617–620.

(11) Mafra, D.; Gava, P.; Malard, L.; Borges, R.; Silva, G.; Leon, J.; Plentz, F.; Mauri, F.; Pimenta, M. Characterizing intrinsic charges in top gated bilayer graphene device by Raman spectroscopy. *Carbon* **2012**, *50*, 3435–3439.

(12) Perdew, J. P.; Burke, K.; Ernzerhof, M. Generalized Gradient Approximation Made Simple. *Phys. Rev. Lett* **1996**, *77*, 3865–3868.

(13) Biswas, S.; Li, Y.; Winter, S. M.; Knolle, J.; Valentí, R. Electronic Properties of $\alpha-RuCl_3$ in Proximity to Graphene. *Phys. Rev. Lett.* **2019**, *123*, 237201.

(14) Grimme, S. Accurate description of van der Waals complexes by density functional theory including empirical corrections. *Journal of Computational Chemistry* **2004**, *25*, 1463–1473.

(15) Sandilands, L. J.; Sohn, C. H.; Park, H. J.; Kim, S. Y.; Kim, K. W.; Sears, J. A.; Kim, Y.-J.; Noh, T. W. Optical probe of Heisenberg-Kitaev magnetism in $\alpha-RuCl_3$. *Phys. Rev. B* **2016**, *94*, 195156.

(16) Tian, Y.; Gao, W.; Henriksen, E. A.; Chelikowsky, J. R.; Yang, L. Optically Driven Magnetic Phase Transition of Monolayer RuCl 3. *Nano Letters* **2019**, *19*, 7673–7680.

(17) Perdew, J. P.; Burke, K.; Ernzerhof, M. Generalized Gradient Approximation Made Simple. *Phys. Rev. Lett.* **1996**, *77*, 3865–3868.

(18) Schlipf, M.; Gygi, F. Optimization algorithm for the generation of ONCV pseudopotentials. *Computer Physics Communications* **2015**, *196*, 36 – 44.

(19) Freysoldt, C.; Boeck, S.; Neugebauer, J. Direct minimization technique for metals in density functional theory. *Phys. Rev. B* **2009**, *79*, 241103.

(20) Sundararaman, R.; Letchworth-Weaver, K.; Schwarz, K. A.; Gunceler, D.; Ozhabes, Y.; Arias, T. JDFTx: Software for joint density-functional theory. *SoftwareX* **2017**, *6*, 278 – 284.

(21) Payne, M. C.; Teter, M. P.; Allan, D. C.; Arias, T. A.; Joannopoulos, J. D. Iterative minimization techniques for ab initio total-energy calculations: molecular dynamics and conjugate gradients. *Rev. Mod. Phys.* **1992**, *64*, 1045–1097.

(22) Katmis, F.; Lauter, V.; Nogueira, F. S.; Assaf, B. A.; Jamer, M. E.; Wei, P.; Satpati, B.; Freeland, J. W.; Eremin, I.; Heiman, D.; Jarillo-Herrero, P.; Moodera, J. S. A high-temperature ferromagnetic topological insulating phase by proximity coupling. *Nature* **2016**, *533*, 513–516.

(23) Merlin, R.; Zeyher, R.; Güntherodt, G. Spin-Disorder-Induced Raman Scattering in Europium Chalcogenides. *Phys. Rev. Lett.* **1977**, *39*, 1215–1218.

(24) Osterhoudt, G. B.; Carelli, R.; Burch, K. S.; Katmis, F.; Gedik, N.; Moodera, J. S. Charge transfer in EuS/Bi_2Se_3 heterostructures as indicated by the absence of Raman scattering. *Phys. Rev. B* **2018**, *98*, 014308.

(25) Shapira, Y.; Reed, T. Resistivity and hall effect of EuS in high magnetic fields. *Physics Letters A* **1971**, *35*, 272 – 273.

(26) Gerber, E.; Yao, Y.; Arias, T. A.; Kim, E.-A. Ab Initio Mismatched Interface Theory of Graphene on $\alpha-RuCl_3$: Doping and Magnetism. *Phys. Rev. Lett.* **2020**, *124*, 106804.

(27) Jones, A. M.; Yu, H.; Ghimire, N. J.; Wu, S.; Aivazian, G.; Ross, J. S.; Zhao, B.; Yan, J.; Mandrus, D. G.; Xiao, D.; Yao, W.; Xu, X. Optical generation of excitonic valley coherence in monolayer WSe2. *Nature Nanotechnology* **2013**, *8*, 634–638.

(28) Chen, J.-W. et al. A gate-free monolayer WSe2 pn diode. *Nature Communications* **2018**, *9*, 3143.

(29) Ma, Q. et al. Giant intrinsic photoresponse in pristine graphene. *Nature Nanotechnology* **2019**, *14*, 145–150.

(30) Wang, Y.-P.; Zhou, H.-J.; Zhao, G.-H.; Xia, T.-L.; Wang, L.; Wang, L.; Zhang, L.-Y. Rapidly counting atomic planes of ultra-thin $MoSe_2$ nanosheets ($1 \leq n \leq 4$) on Si_2/Si substrate. *Rare Metals* **2016**, *35*, 632–636.

(31) Zhou, B.; Balgley, J.; Lampen-Kelley, P.; Yan, J.-Q.; Mandrus, D. G.; Henriksen, E. A. Evidence for charge transfer and proximate magnetism in graphene-α-$RuCl_3$heterostructures. *Phys. Rev. B* **2019**, *100*, 165426.

(32) Mashhadi, S.; Kim, Y.; Kim, J.; Weber, D.; Taniguchi, T.; Watanabe, K.; Park, N.; Lotsch, B.; Smet, J. H.; Burghard, M.; Kern, K. Spin-Split Band Hybridization in Graphene Proximitized with α-RuCl3 Nanosheets. *Nano Letters* **2019**, *19*, 4659–4665.

(33) Efetov, D. K.; Kim, P. Controlling Electron-Phonon Interactions in Graphene at Ultrahigh Carrier Densities. *Phys. Rev. Lett.* **2010**, *105*, 256805.

(34) Ye, J.; Craciun, M. F.; Koshino, M.; Russo, S.; Inoue, S.; Yuan, H.; Shimotani, H.; Morpurgo, A. F.; Iwasa, Y. Accessing the transport properties of graphene and its multilayers at high carrier density. *Proceedings of the National Academy of Sciences* **2011**, *108*, 13002–13006.

(35) Pachoud, A.; Jaiswal, M.; Ang, P. K.; Loh, K. P.; Özyilmaz, B. Graphene transport at high carrier densities using a polymer electrolyte gate. *EPL (Europhysics Letters)* **2010**, *92*, 27001.

(36) Bruna, M.; Ott, A. K.; Ijäs, M.; Yoon, D.; Sassi, U.; Ferrari, A. C. Doping Dependence of the Raman Spectrum of Defected Graphene. *ACS Nano* **2014**, *8*, 7432–7441.

(37) Chen, F.; Qing, Q.; Xia, J.; Li, J.; Tao, N. Electrochemical Gate-Controlled Charge Transport in Graphene in Ionic Liquid and Aqueous Solution. *Journal of the American Chemical Society* **2009**, *131*, 9908–9909.

(38) Browning, A.; Kumada, N.; Sekine, Y.; Irie, H.; Muraki, K.; Yamamoto, H. Evaluation of disorder introduced by electrolyte gating through transport measurements in graphene. *Applied Physics Express* **2016**, *9*, 065102.

(39) Saha, S.; Kahya, O.; Jaiswal, M.; Srivastava, A.; Annadi, A.; Balakrishnan, J.; Pachoud, A.; Toh, C.-T.; Hong, B.-H.; Ahn, J.-H.; Venkatesan, T.; Özyilmaz, B. Unconventional Transport through Graphene on SrTiO3: A Plausible Effect of SrTiO3 Phase-Transitions. *Scientific Reports* **2015**, *4*, 6173.

(40) Zhao, W.; Tan, P. H.; Liu, J.; Ferrari, A. C. Intercalation of Few-Layer Graphite Flakes with FeCl3: Raman Determination of Fermi Level, Layer by Layer Decoupling, and Stability. *Journal of the American Chemical Society* **2011**, *133*, 5941–5946.

(41) Grüneis, A.; Attaccalite, C.; Rubio, A.; Vyalikh, D. V.; Molodtsov, S. L.; Fink, J.; Follath, R.; Eberhardt, W.; Büchner, B.; Pichler, T. Angle-resolved photoemission study of the graphite intercalation compound KC_8: A key to graphene. *Phys. Rev. B* **2009**, *80*, 075431.

(42) Elias, J. A.; Henriksen, E. A. Unexpected Hole Doping of Graphene by Osmium Adatoms. *Annalen der Physik* **2020**, *532*, 1900294.

(43) Elias, J. A.; Henriksen, E. A. Electronic transport and scattering times in tungsten-decorated graphene. *Phys. Rev. B* **2017**, *95*, 075405.

(44) Chandni, U.; Henriksen, E. A.; Eisenstein, J. P. Transport in indium-decorated graphene. *Phys. Rev. B* **2015**, *91*, 245402.

(45) McChesney, J. L.; Bostwick, A.; Ohta, T.; Seyller, T.; Horn, K.; González, J.; Rotenberg, E. Extended van Hove Singularity and Superconducting Instability in Doped Graphene. *Phys. Rev. Lett.* **2010**, *104*, 136803.

(46) Zhang, X.; Hsu, A.; Wang, H.; Song, Y.; Kong, J.; Dresselhaus, M. S.; Palacios, T. Impact of Chlorine Functionalization on High-Mobility Chemical Vapor Deposition Grown Graphene. *ACS Nano* **2013**, *7*, 7262–7270.